J|A|C|S ARTICLES

Published on Web 09/03/2010

Relating *n*-Pentane Isomerization Activity to the Tungsten Surface Density of WO_x/ZrO_2

Nikolaos Soultanidis,[†] Wu Zhou,[‡] Antonis C. Psarras,[§] Alejandro J. Gonzalez,[||] Eleni F. Iliopoulou,[§] Christopher J. Kiely,[‡] Israel E. Wachs,[⊥] and Michael S. Wong*[,†,#]

Department of Chemical and Biomolecular Engineering, Rice University, Houston, Texas 77005, Department of Materials Science and Engineering, Lehigh University, Bethlehem, Pennsylvania 18015, Laboratory of Environmental Fuels and Hydrocarbons, Chemical Process Engineering Research Institute/Center of Research and Technology Hellas, Thessaloniki, Greece, Research Department, DCG Partnership, Pearland, Texas 77581, Operando Molecular Spectroscopy and Catalysis Laboratory, Department of Chemical Engineering, Lehigh University, Bethlehem, Pennsylvania 18015, and Department of Chemistry, Rice University, Houston, Texas 77005

Received June 23, 2010; E-mail: mswong@rice.edu

Abstract: Zirconia-supported tungsten oxide (WO_x/ZrO_2) is considered an important supported metal oxide model acid catalyst, for which structure−property relationships have been studied for numerous acid-catalyzed reactions. The catalytic activity for xylene isomerization, alcohol dehydration, and aromatic acylation follows a volcano-shape dependence on tungsten surface density. However, WO_x/ZrO_2 has not been studied for more acid-demanding reactions, like *n*-pentane isomerization, with regard to surface density dependence. In this work, WO_x/ZrO_2 was synthesized using commercially available amorphous $ZrO_x(OH)_{4-2x}$ and model crystalline ZrO_2 as support precursors. They were analyzed for *n*-pentane isomerization activity and selectivity as a function of tungsten surface density, catalyst support type, and calcination temperature. Amorphous $ZrO_x(OH)_{4-2x}$ led to WO_x/ZrO_2 (WZrOH) that exhibited maximum isomerization activity at ∼5.2 $W \cdot nm^{-2}$, and the crystalline ZrO_2 led to a material ($WZrO_2$) nearly inactive at all surface densities. Increasing the calcination temperature from 773 to 973 K increased the formation of 0.8−1 nm Zr-WO_x clusters detected through direct imaging on an aberration-corrected high-resolution scanning transmission electron microscope (STEM). Calcination temperature further increased catalytic activity by at least two times. Brønsted acidity was not affected but Lewis acidity decreased in number, as quantified via pyridine adsorption infrared spectroscopy. WO_x/ZrO_2 exhibited isomerization activity that peaked within the first 2 h time-on-stream, which may be due to Zr-WO_x clusters undergoing an activation process.

1. Introduction

Supported metal oxide catalysts comprise an important class of industrial catalytic materials, with tungstated zirconia (WO_x/ZrO_2) representing an important model for an acid catalytic material.[1−5] It is strongly acidic and structurally more stable than sulfated zirconia and chlorided Pt/Al_2O_3, which can release H_2S and HCl during reaction and regeneration conditions.[5−7]

Structure−activity correlations for WO_x/ZrO_2 have been studied actively by several research groups. Santiesteban and co-workers attributed the balance between *in situ* strong Brønsted and Lewis sites to the high *n*-pentane isomerization activity observed at intermediate tungsten oxide loadings.[8−10] Knözinger and co-workers proposed that Zr^{4+}-exposed WO_x polytungstates generated strong Brønsted acidity for structures similar to that of heteropolyacids.[11−13] *o*-Xylene isomerization and 2-butanol dehydration activity were investigated by Iglesia and co-workers, who proposed that the slight reduction of surface polytungstate species formed *in situ* Brønsted acid sites, of which maximum activity was found at ∼7−8 $W \cdot nm^{-2}$.[5,14−18] Most recently, Ross-Medgaarden et al. proposed a model in

[†] Department of Chemical and Biomolecular Engineering, Rice University.
[‡] Department of Materials Science & Engineering, Lehigh University.
[§] Chemical Process Engineering Research Institute/Center of Research and Technology Hellas.
[||] DCG Partnership.
[⊥] Lehigh University.
[#] Rice University.

(1) Hino, M.; Arata, K. *J. Chem. Soc., Chem. Commun.* **1988**, *18*, 1259.
(2) Hino, M.; Arata, K. *Chem. Lett.* **1989**, *6*, 971.
(3) Barton, D. G.; Soled, S. L.; Iglesia, E. *Top. Catal.* **1998**, *6*, 87–99.
(4) Ross-Medgaarden, E. I.; Knowles, W. V.; Kim, T.; Wong, M. S.; Zhou, W.; Kiely, C. J.; Wachs, I. E. *J. Catal.* **2008**, *256*, 108–125.
(5) Barton, D. G.; Soled, S. L.; Meitzner, G. D.; Fuentes, G. A.; Iglesia, E. *J. Catal.* **1999**, *181*, 57–72.
(6) Thomas, J. M. *Sci. Am.* **1992**, *266*, 112–118.
(7) Corma, A. *Catal. Lett.* **1993**, *22*, 33–52.
(8) Santiesteban, J. G.; Vartuli, J. C.; Han, S.; Bastian, R. D.; Chang, C. D. *J. Catal.* **1997**, *168*, 431–441.
(9) Vartuli, J. C.; Santiesteban, J. G.; Traverso, P.; Cardona-Martinéz, N.; Chang, C. D.; Stevenson, S. A. *J. Catal.* **1999**, *187*, 131–138.
(10) Calabro, D. C.; Vartuli, J. C.; Santiesteban, J. G. *Top. Catal.* **2002**, *18*, 231–242.
(11) Kuba, S.; Lukinskas, P.; Ahmad, R.; Jentoft, F. C.; Grasselli, R. K.; Gates, B. C.; Knözinger, H. *J. Catal.* **2003**, *219*, 376–388.
(12) Scheithauer, M.; Cheung, T. K.; Jentoft, R. E.; Grasselli, R. K.; Gates, B. C.; Knözinger, H. *J. Catal.* **1998**, *180*, 1–13.
(13) Scheithauer, M.; Grasselli, R. K.; Knozinger, H. *Langmuir* **1998**, *14*, 3019–3029.
(14) Wilson, R. D.; Barton, D. G.; Baertsch, C. D.; Iglesia, E. *J. Catal.* **2000**, *194*, 175–187.

10.1021/ja105519y

which maximum methanol dehydration activity observed at surface densities of 6−7 $W \cdot nm^{-2}$ was attributed to high concentrations of 0.8−1.0 nm Zr-containing WO_x three-dimensional ("Zr−WO_x") clusters,[4] which was later confirmed by Zhou et al. via direct imaging of all the surface WO_x species using aberration-corrected STEM high-angle annular dark-field (HAADF) imaging.[19] The surface acid sites active for this reaction are presumably weaker than those required for more acid-demanding reactions like alkane isomerization and cracking.[20,21] However, systematic investigation of WO_x/ZrO_2 catalysts for *n*-pentane isomerization, a more acid-demanding reaction, as a function of WO_x surface density has not been reported before.

In this work, we report the catalytic properties as a function of tungsten surface density and deduce the structure−activity relationship in supported WO_x/ZrO_2 solid acid catalysts for *n*-pentane isomerization. Amorphous and crystalline zirconia materials were used as support to prepare the WO_x/ZrO_2 catalysts through incipient wetness impregnation, which allowed us to investigate the effect of the support material on the nature of the active sites. The atomic structure of various surface WO_x species was characterized by aberration-corrected STEM-HAADF imaging. We assessed surface acidity through pyridine adsorption FTIR studies.

2. Experimental Methods

2.1. Catalyst Preparation. All catalysts were synthesized by incipient wetness impregnation of an aqueous solution of ammonium metatungstate ($(NH_4)_6H_2W_{12}O_{40} \cdot 5H_2O$, AMT) into (1) amorphous zirconium oxyhydroxide ($ZrO_x(OH)_{4-2x}$, MEI XZO 880/01) and (2) model crystalline zirconium oxide (ZrO_2, Degussa) supports. These two supports were initially sieved (−170 mesh) and mixed overnight using an automated VWR rocking platform. The amorphous $ZrO_x(OH)_{4-2x}$ was found to have a specific surface area (SSA) of 330 $m^2 \cdot g^{-1}$ and pore volume of 0.33 $cm^3 \cdot g^{-1}$, while the crystalline ZrO_2 support was found to have a specific surface area of 58 $m^2 \cdot g^{-1}$ and pore volume of 0.15 $cm^3 \cdot g^{-1}$, as determined from nitrogen physisorption analysis of three different batches of each support type.

Prior to impregnation, the support was degassed in a vacuum oven overnight at a moderate temperature (343 K) in order to remove the excess moisture without causing any significant structural changes. Aqueous solutions of AMT (Aldrich), with different tungsten oxide loadings, were impregnated up to 95% of the pore volume of the support. A correction to the calculated aqueous AMT solution volume was applied prior to impregnation according to previously reported observations[22] to ensure accuracy. After impregnation, all samples were hand mixed and dried at 343 K overnight in static air. Samples were then crushed, sieved, and finally heated up at a ramp rate of 3.0 $K \cdot min^{-1}$ under flowing air (100 $cm^3 \cdot min^{-1}$) and calcined at the desired calcination temperature for 3 h. Crushing and sieving were repeated once more to acquire a fine powder with a catalyst particle size of 150 μm or less (−170 mesh). This powder was then pelletized, crushed, and sieved into the 300−600 μm range for all catalytic reaction experiments (Supporting Information).

The following sample notations are employed in this paper. ρ_{surf}−WZrOH(z,T) refers to AMT-impregnated amorphous $ZrO_x(OH)_{4-2x}$, where ρ_{surf} is the surface density calculated using the surface area of the catalyst after calcination ($W \cdot nm^{-2}$),[4,22,23] z is the tungsten oxide weight loading (wt% of WO_3), and T is the calcination temperature (K). For the samples supported on model crystalline ZrO_2 the nomenclature used was ρ_{surf}−$WZrO_2$(z,T). A simplified notation is used when referring to a specific series of samples, namely WZrOH(T) and $WZrO_2$(T). Bulk WO_3 powder (Sigma) was used without further purification as a control sample.

2.2. Catalyst Characterization. Nitrogen physisorption studies were performed on Micromeritics ASAP 2010 using Matheson ultrahigh purity (UHP) nitrogen. All synthesized samples with the exception of the amorphous support were evacuated for more than 4 h at 523 K until the degas rate was less than 4×10^{-3} $mmHg \cdot min^{-1}$.

X-ray diffraction (XRD) patterns were acquired on a Rigaku D/Max-2100PC using a continuous scanning mode[4] with a 0.02° step size and a scan rate of 2.5 $s \cdot step^{-1}$.

Bright field (BF) images, selective area diffraction (SAD), and X-ray energy dispersive spectroscopy (XEDS) of the samples were obtained using a JEOL 2000FX TEM operating at 200 kV. High resolution TEM (HRTEM) imaging and high-angle annular dark field (HAADF) imaging[24] were performed on a 200 kV JEOL 2200FS (S)TEM equipped with a CEOS probe C_s-corrector at Lehigh University. The HAADF images presented have been low-pass filtered to reduce background noise. The catalyst samples were also characterized by secondary electron (SE) imaging and back-scattered electron (BSE) imaging on a Hitachi 4300LV scanning electron microscope (SEM). Samples suitable for SEM analysis were made by directly dispersing the catalyst powder onto carbon tape and coated with iridium (Ir) to mitigate charging effects.

Qualitative and quantitative acid site measurements were performed on a Nicolet 5700 FTIR spectrometer using an MCT-A detector and a homemade stainless steel, vacuum cell, with CaF_2 windows.[25] Lewis (L) and Brønsted (B) site concentrations were calculated according to the Beer−Lambert law corrected with the normalized weight of the wafers, with a radius of 0.405 cm and thickness of ~1 mm. The molar extinction coefficients of 1.67 and 2.22 $cm \cdot \mu mol^{-1}$ for the L and B sites, respectively, were used.[26] The weak and moderate acid sites were quantified by the amount of pyridine desorbed in the ranges of 423−523 K and 523−723 K; the amount of undesorbed pyridine quantified the amount of strong acid sites. For each temperature, the sample was cooled down and spectra were collected at 423 K to avoid inconsistencies caused by band broadening and intensity amplification at elevated temperatures. L and B acid site concentrations were expressed in two ways: (1) in micromoles of chemisorbed Py per gram of catalyst and (2) in sites per W atom.[9,14]

2.3. Catalytic Studies. The catalytic studies were performed on an isothermal downflow reactor at 523 K, with an internal diameter (ID) of 6.26 mm, packed with ~0.33 g of catalyst (particle size in the 300−600 μm range). The catalyst bed length was fixed to be 2.22 cm long by adjusting the catalyst loading ±0.02 g in order to ensure a constant gas-hourly space velocity (GHSV = 68). GHSV is equal to u_0/V, where $u_0 = 0.78$ $mL \cdot min^{-1}$ is the volumetric flow

(15) Baertsch, C. D.; Komala, K. T.; Chua, Y.-H.; Iglesia, E. *J. Catal.* **2002**, *205*, 44–57.
(16) Baertsch, C. D.; Soled, S. L.; Iglesia, E. *J. Phys. Chem. B* **2001**, *105*, 1320–1330.
(17) Baertsch, C. D.; Wilson, R. D.; Barton, D. G.; Soled, S. L.; Iglesia, E. *Stud. Surf. Sci. Catal.* **2000**, *130D*, 3225–3230.
(18) Barton, D. G.; Shtein, M.; Wilson, R. D.; Soled, S. L.; Iglesia, E. *J. Phys. Chem. B* **1999**, *103*, 630–640.
(19) Zhou, W.; Ross-Medgaarden, E. I.; Knowles, W. V.; Wong, M. S.; Wachs, I. E.; Kiely, C. J. *Nat. Chem.* **2009**, *1*, 722–728.
(20) Corma, A. *Chem. Rev.* **1995**, *95*, 559–614.
(21) Corma, A. *Curr. Opin. Solid State Mater. Sci.* **1997**, *2*, 63–75.
(22) Knowles, W. V.; Nutt, M. O.; Wong, M. S. *Supported Metal Oxides and Surface Density Metric*; Taylor and Francis: Boca Raton, FL, 2006; Chapter 11.
(23) Soultanidis, N.; Knowles, W. V.; Ross-Medgaarden, E. I.; Wachs, I. E.; Wong, M. S. In preparation.
(24) Nellist, P. D.; Pennycook, S. J. *Science* **1996**, *274*, 413–415.
(25) Psarras, A. C.; Iliopoulou, E. F.; Kostaras, K.; Lappas, A. A.; Pouwels, C. *Microporous Mesoporous Mater.* **2009**, *120*, 141–146.
(26) Emeis, C. A. *J. Catal.* **1993**, *141*, 347–354.
(27) Macht, J.; Baertsch, C. D.; May-Lozano, M.; Soled, S. L.; Wang, Y.; Iglesia, E. *J. Catal.* **2004**, *227*, 479–491.

rate measured at standard temperature and pressure (STP) and $V = 0.68$ mL is the volume of the catalytic bed.

Prior to each reaction run, samples were pretreated *in situ* at 673 K under a continuous flow (100 $cm^3 \cdot min^{-1}$) of ultrahigh purity (UHP) air for 1 h. Then, the reactor was cooled down to 523 K under flowing UHP He (100 $cm^3 \cdot min^{-1}$) in order to remove any physisorbed oxygen. The reactor feed gas was a blend of 1% *n*-pentane and 1% argon in helium (prepared by gravimetric blending).

The duration of all runs presented in this paper was 10 h, during which a chromatogram was collected every 23 min. For calculating the partial *n*-pentane conversion to the various products, a carbon mass balance approach was used (eq 1) similar to the one presented by Kuba et al.[11]

$$x_i = \frac{(i/5)C_i}{nC_{5\text{in}}} \quad (1)$$

where $i = 1-6$ is the number of carbon atoms of each product from methane to C_6 olefins and hexane, C_i is the moles of each product, and $nC_{5_{in}}$ is the moles of *n*-pentane (nC_5) fed to the reactor. After normalizing with respect to the internal standard concentration, the total conversion X [(mol of *n*-pentane converted)$\cdot$(mol of *n*-pentane fed)$^{-1}$] was calculated by using eq 2.

$$X = \frac{\sum_{i=1}^{6}(i/5)C_i}{nC_{5\text{in}}} \quad (2)$$

Selectivity for each product is defined as S_i [(conversion of i product)$\cdot$(total conversion)$^{-1}$]

$$S_i = \frac{x_i}{X} \quad (3)$$

Since the total conversion remained low ($\leq$3%) for all runs, the conditions were considered to be differential, and therefore the total conversion rate of nC_5, R_{nC5} [(mol of nC_5 converted)$\cdot$(g of catalyst$\cdot$s)$^{-1}$], could be expressed as

$$R_{nC_5} = \frac{F_{nC_5}X}{W_{cat}} \quad (4)$$

where F_{nC_5} [(mol of nC_5)$\cdot s^{-1}$] is the steady-state molar flow rate of nC_5 and W_{cat} [g] is the amount of catalyst used for each run.

In comparing the activity for the catalyst samples, the nC_5 consumption turnover rate TOR [s^{-1}] and the isomerization turnover rate TOR_{iC_5} [s^{-1}] were used, which respectively represented the number of nC_5 molecules reacted per tungsten atom$\cdot$per second (eq 5) and the number nC_5 molecules isomerized into isopentane (iC_5) per tungsten atom$\cdot$per second (eq 6).

$$\text{TOR} = \frac{(R_{nC_5})(N_A)}{(N_s)(\text{SSA})(10^{18})} \quad (5)$$

$$\text{TOR}_{iC_5} = S_{iC_5}\text{TOR} \quad (6)$$

where N_A is Avogadro's number, SSA is the BET specific surface area, and N_s [sites$\cdot nm^{-2}$] is the active site surface density.[4,22,23] N_s was assumed to be numerically equivalent to ρ_{surf}. However, it should be noted that TOR would not represent a true turnover frequency above WO_x monolayer (ML) coverage, i.e., $\rho_{surf} > 4.5$ W$\cdot nm^{-2}$, [4,8,18,27] because the tungsten oxide content would not be 100% accessible for reaction. For the rest of the products, cracking and oligomerization selectivities were calculated using $i = 1-4$ and $i > 5$, respectively. Steady-state TORs and selectivities were collected at $t = 10$ h.

Table 1. BET Surface Area, Pore Volume, and Calculated Tungsten Surface Density Values of Various Supported WO_x/ZrO_2 Catalysts

Catalyst sample (WO_3 wt %, calcination temperature K)	BET SSA [$m^2 \cdot g^{-1}$]	Pore volume [$cm^3 \cdot g^{-1}$]	Surface density ρ_{surf} [W$\cdot nm^{-2}$]	Surface density ρ_{surf} [W$\cdot nm_{supp}^{-2}$]
2.5−WZrOH (7.0, 973)	72.0	0.185	2.5	2.8
3.6−WZrOH (13.2, 973)	92.3	0.183	3.6	5.2
5.2−WZrOH (18.5, 973)	93.0	0.199	5.2	7.6
6.0−WZrOH (21.7, 973)	95.5	0.210	6.0	8.8
8.5−WZrOH (30.0, 973)	92.0	0.204	8.5	12.0
11.0−WZrOH (32.4, 973)	76.0	0.168	11.0	13.0
2.2−WZrOH (9.2, 773)	109.0	0.230	2.2	2.9
3.5−WZrOH (18.5, 773)	138.0	0.218	3.5	6.0
4.4−WZrOH (21.7, 773)	128.0	0.206	4.4	7.1
8.0−WZrOH (30.0, 773)	98	0.185	8.0	9.5
2.2−$WZrO_2$ (4.8, 773)	56.0	0.195	2.2	2.2
3.5−$WZrO_2$ (7.0, 773)	53.0	0.165	3.5	3.2
4.4−$WZrO_2$ (8.8, 773)	52.0	0.163	4.4	4.0
6.1−$WZrO_2$ (12.2, 773)	52.0	0.147	6.1	5.5

3. Results and Discussion

3.1. Catalyst Structure. The SSA and V_p for the catalyst samples are summarized in Table 1. Surface tungsten oxide density values were calculated in two ways: (1) using the measured SSA of the catalysts after calcination, to give units of W$\cdot nm^{-2}$, and (2) using the SSA of the support materials ($ZrO_x(OH)_{4-2x}$ or ZrO_2) after calcination, to give units of W$\cdot nm_{supp}^{-2}$ (Table 1). These calculations gave similar values for low tungsten oxide content and differed significantly at high tungsten oxide content.[4,22]

The SSA of WZrOH samples increased to a maximum before decreasing with tungsten oxide loading, which is consistent with the reported thermal stabilizing role of WO_x on the amorphous $ZrO_x(OH)_{4-2x}$ support during calcination.[13,16,23] The SSA of the model $WZrO_2$ materials, however, was not affected much by the calcination.

The XRD patterns for the WZrOH(973) material are presented in Figure 1. All samples calcined at 973 K were crystalline with both tetragonal ("t-ZrO_2") and monoclinic ("m-ZrO_2") zirconia phases. Monoclinic WO_3 ("m-WO_3") crystals were also detected at higher ρ_{surf}. The observed trends were in agreement with published reports that indicated the ability of WO_x to retard the phase transformation of t-ZrO_2 to the thermodynamically more stable m-ZrO_2 phase.[4,5,13] XRD peaks for the m-WO_3 crystal phase were seen to emerge at a surface density between 3.6 and 5.2 W$\cdot nm^{-2}$, which was lower than 7−8 W$\cdot nm^{-2}$ observed by others.[4,18] Bulk WO_3 formed at a lower surface density than expected, perhaps due to incomplete spreading of the meta-tungstate salt solution over the $ZrO_x(OH)_{4-2x}$ support during the impregnation process.[23]

In contrast to the observations made for the WZrOH samples calcined at 973 K, the WZrOH samples calcined at 773 K appeared to be mostly amorphous at low ρ_{surf}, and no m-ZrO_2 was formed in samples with W surface densities below 8.0 W$\cdot nm^{-2}$; WO_3 crystals were not detected in any of the WZrOH(773) catalysts. The WO_x species in these samples were therefore expected to be monotungstates and polytungstates species.[23,28−30]

(28) Wachs, I. E.; Kim, T.; Ross, E. I. *Catal. Today* **2006**, *116*, 162–168.

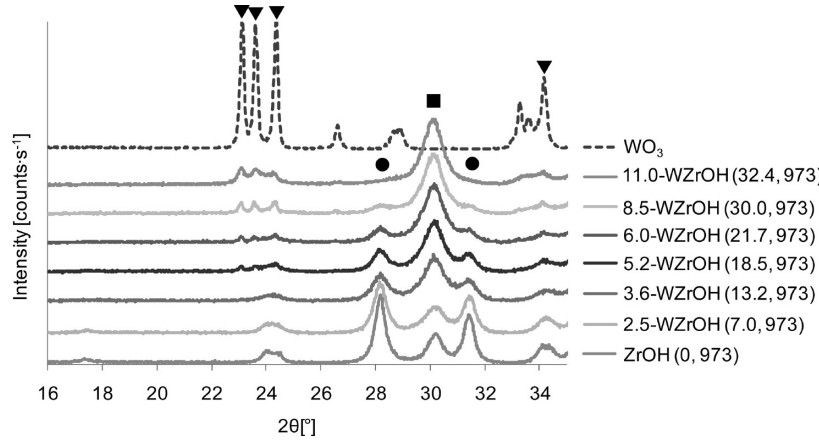

Figure 1. Powder XRD patterns of WZrOH and $Zr_x(OH)_{4-2x}$ calcined at 973 K and bulk WO_3. Crystalline phases marked as (▼) m-WO_3, (●) m-ZrO_2, and (■) t-ZrO_2.

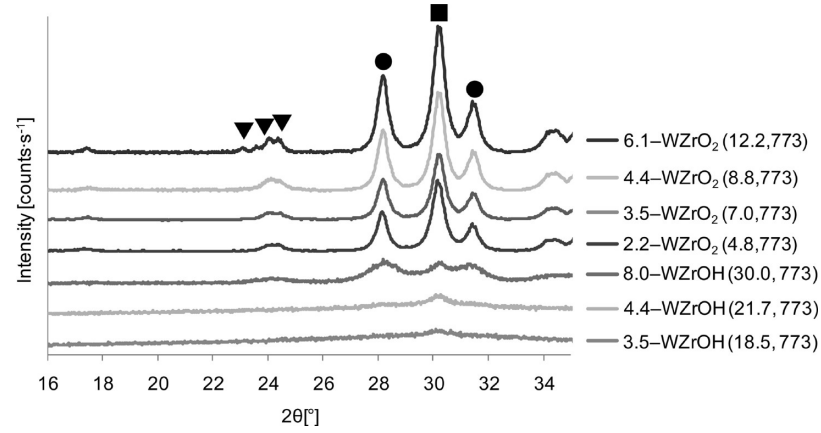

Figure 2. Powder XRD patterns of $WZrO_2$(773) and WZrOH(773). Crystalline phases marked as (▼) m-WO_3, (●) m-ZrO_2, and (■) t-ZrO_2.

The crystal structure of the ZrO_2 support in the $WZrO_2$ catalysts remained similar at all of the investigated WO_x surface densities, and a small fraction of WO_3 crystals were observed in the 6.1$WZrO_2$ (12.2, 773) catalyst (Figure 2).

3.2. Electron Microscopy Analysis. 3.2.1. Catalyst with Low WO_x Loading below Monolayer Coverage. Bright field (BF) TEM imaging was used to characterize the morphology of the catalyst samples. As shown in Figure 3a, two distinct morphologies were observed in the 2.5−WZrOH (7.0, 973) catalyst: agglomerates of smaller (5−12 nm) ZrO_2 particles (labeled X) and agglomerates of larger (15−40 nm) ZrO_2 particles (labeled Y). The HRTEM image of a typical larger ZrO_2 particle (Figure 3b) shows clear lattice fringes extending right out to the surface of the grain, indicating a loading below the surface WO_x monolayer coverage. In contrast, some dark speckles can be seen (Figure 3c) at the boundaries and surface of the aggregates of the smaller ZrO_2 particles, which can be caused by either amorphous interfacial films or clusters on the surface.

The structure and distribution of WO_x surface species were investigated using HAADF-STEM imaging, which provides *Z*-contrast information. In Figure 3d, the heavier W atoms show up as very bright spots while the ZrO_2 crystals show a fainter lattice fringe contrast. Features corresponding to surface monotungstate (i.e., isolated W atoms as circled in blue) and surface

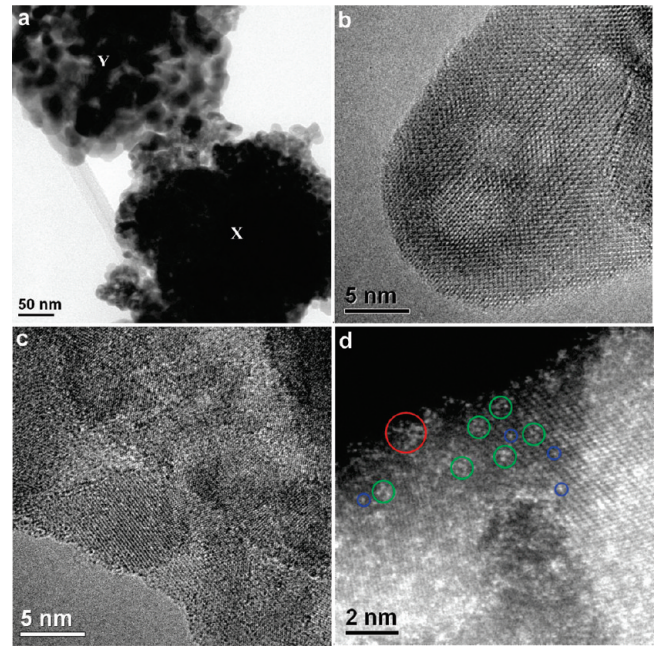

Figure 3. Representative (a) TEM BF, (b, c) HRTEM, and (d) HAADF-STEM images of the supported 2.5−WZrOH (7.0, 973) catalyst. Blue circles: surface monotungstate species; Green circles: surface polytungstate species; Red circles: sub-nm Zr-WO_x clusters.

polytungstate (i.e., interconnected two-dimensional WO_x species with W atoms linked by oxygen bridging bonds as circled in green) are visible on both ZrO_2 morphologies. This observed

(29) Ross-Medgaarden, E. I.; Wachs, I. E. *J. Phys. Chem. C* **2007**, *111*, 15089–15099.
(30) Kim, D. S.; Ostromecki, M.; Wachs, I. E. *J. Mol. Catal A: Chem.* **1996**, *106*, 93–102.

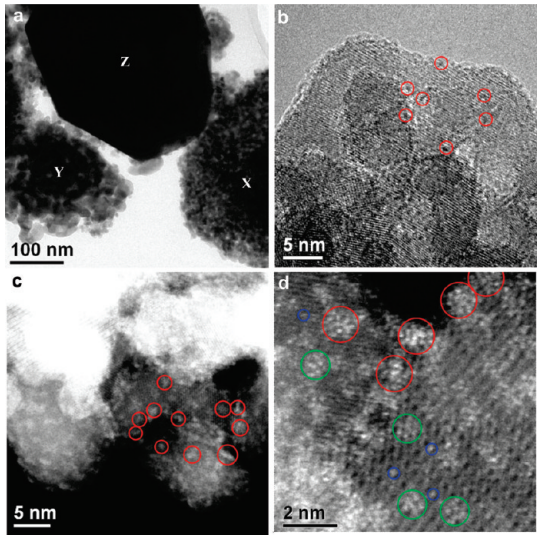

Figure 4. Representative (a) TEM B, (b) HRTEM, and (c, d) HAADF-STEM images of the supported 5.2−WZrOH (18.5, 973) catalyst. Blue circles: surface monotungstate species; Green circles: surface polytungstate species; Red circles: sub-nm Zr-WO_x clusters.

coexistence of surface mono- and polytungstate species at this low surface density (2.5 $W \cdot nm^{-2}$) sample suggests that polytungstate species begin to emerge at a WO_x coverage lower than 2.5 $W \cdot nm^{-2}$, consistent with previous UV−vis spectroscopy results (1.7 $W \cdot nm^{-2}$)[4] and counter to the ∼4.0 $W \cdot nm^{-2}$ value concluded by others.[18] The surface W atoms were found to sit preferentially above the Zr atom columns; this phenomenon becomes clearer when the ZrO_2 crystal is oriented along a major zone axis as in the upper right-hand side particle in Figure 3d. This preferential location of W atoms has been proposed[19] to be a consequence of the strong interaction between WO_x species and surface defect sites on the ZrO_2 support. Although the nominal WO_x surface coverage of this catalyst was below the ML, occasional sub-nm clusters were still found (circled in red in Figure 3d) especially at the intersections of adjacent small ZrO_2 support particles and at the edge of surface pits. The formation of such WO_x clusters at particle boundaries is presumably due to capillary effects, while the edge of surface pits provides a large number of step edge sites for trapping WO_x species. It is important to note that these sub-nm clusters were exclusively found to be associated with the agglomerates of smaller ZrO_2 particles (i.e., X morphology) with a very low number density. Thus, the larger particles (i.e., Y morphology) were possibly formed as a consequence of local inhomogeneities in the WO_x distribution and calcination conditions.

3.2.2. Catalyst with WO_x Loading Close to Monolayer Coverage. Three different morphologies were found in 5.2−WZrOH (18.5, 973) (Figure 4a). The first morphology (labeled X) consists of agglomerates of small (5−12 nm) ZrO_2 support particles; the second morphology (labeled Y) consists of clumps of larger (15−50 nm) ZrO_2 support particles; the third distinct morphology (labeled Z) is comprised of large isolated single crystalline particles up to a few hundred nanometers in size. The X and Y morphologies are similar to those found in the low loading catalyst, but with a smaller volume fraction of morphology Y, which is consistent with the slight peak broadening noted in the corresponding XRD spectrum. Evidence of internal voids and/or surface pits due to the loss of water from the $ZrO_x(OH)_{4-2x}$ precursor material during calcination of the support could be seen in both ZrO_2 morphologies, which again serve as preferential sites for WO_x cluster nucleation.

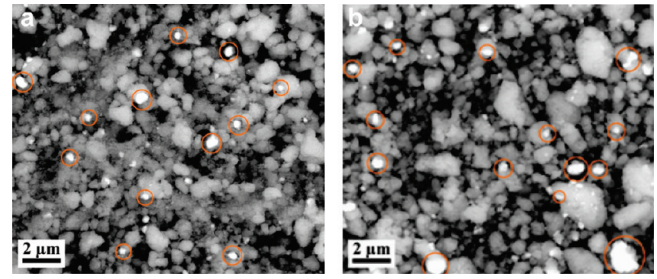

Figure 5. Representative (a) SEM BSE images of 5.2−WZrOH (18.5, 973) and (b) 8.5−WZrOH (30.0, 973). WO_3 crystals a few hundred nanometers in size are circled.

Sub-nm dark flecks can be seen in both ZrO_2 morphologies in HRTEM images (Figure 4b). However, an accurate evaluation of the size and number density of these clusters is only possible from a lower magnification HAADF-STEM image (Figure 4c) which shows a high number density of 0.8−1 nm clusters. The high resolution HAADF image (Figure 4d) shows the WO_x clusters having a considerably higher image contrast as compared with the monotungstate and polytungstate species, confirming that these WO_x clusters are three-dimensional in nature with a thickness of 2−3 atomic layers. A rough estimate, based on the size of the clusters, suggests that each cluster should contain between 10 and 20 WO_x structural units (as compared to 2−6 WO_x structural units in the polytungstate species). Zhou et al. explained that subtle contrast variations observed within a single cluster in HAADF images were most likely caused by the intermixing of a small amount of ZrO_x species within these WO_x clusters to form the catalytically active Zr-WO_x clusters.[19] The grain boundary grooves between intersecting ZrO_2 particles again served as preferential sites for WO_x clustering, but the overall increase in WO_x loading saturated the ZrO_2 surface and formed a high number density of these Zr-WO_x clusters. The Zr-WO_x clusters found in this more highly loaded sample had a larger average domain size (Figure 4d) compared to those found in the lower loaded 2.5−WZrOH (7.0, 973) sample.

The much larger particles (labeled Z in Figure 4a) were identified using EDS and electron diffraction techniques to be WO_3 crystals, which were identified to be the monoclinic phase via XRD (Figure 1). Backscattered electron (BSE) imaging in SEM also contains *Z*-contrast information and can be used to locate the WO_3 crystals in the WO_x/ZrO_2 catalysts due to their higher atomic number. SEM BSE images from the 5.2−WZrOH (18.5, 973) catalyst sample (Figure 5a) clearly reveal the distribution of 200−600 nm WO_3 crystals in the sample. These bulk WO_3 crystals are known to possess very low activity for methanol dehydration.[4,31]

3.2.3. Catalyst with WO_x Loading above Monolayer Coverage. Similar to the 5.2−WZrOH (18.5, 973) sample, the three distinct morphologies (X, Y, and Z) were also observed in the 8.5−WZrOH (30.0, 973) catalyst. The two ZrO_2 morphologies (X and Y) are shown in Figure 6a. The larger Y-type ZrO_2 particles appeared even less frequently when compared with the two samples discussed previously. The increase in WO_x loading tended to inhibit the sintering of the ZrO_2 support particles and stabilized the smaller metastable tetragonal ZrO_2 polymorphs, as indicated by the peak broadening and increase in signals for the tetragonal ZrO_2 phase in the XRD spectrum.

A high number density of sub-nm Zr-WO_x clusters were also observed in this sample using both HRTEM and HAADF-STEM

(31) Kim, T.; Burrows, A.; Kiely, C. J.; Wachs, I. E. *J. Catal.* **2007**, *246*, 370–381.

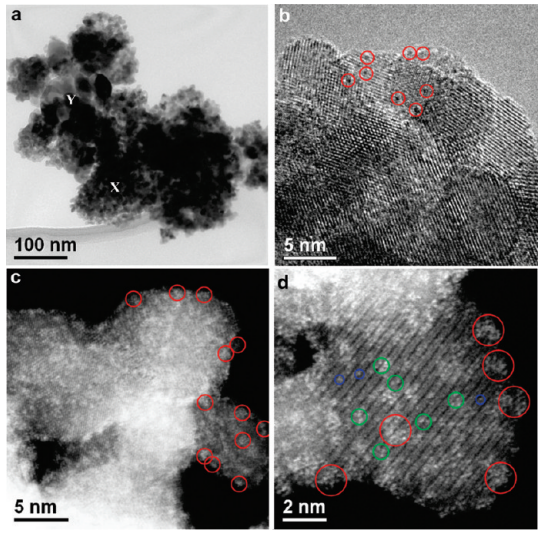

Figure 6. Representative (a) TEM BF, (b) HRTEM, and (c, d) HAADF-STEM images of the supported 8.5−WZrOH (30.0, 973) catalyst. Blue circles: surface monotungstate species; Green circles: surface polytungstate species; Red circles: sub-nm Zr-WO_x clusters.

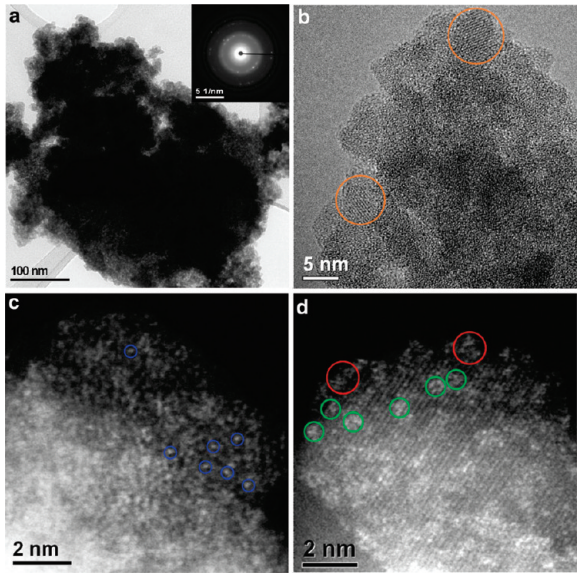

Figure 7. Representative (a) TEM BF, (b) HRTEM, and (c, d) HAADF-STEM images of the supported 4.4−WZrOH (21.7, 773) catalyst. Blue circles: surface monotungstate species; Green circles: surface polytungstate species; Red circles: sub-nm Zr-WO_x clusters.

imaging (Figure 6b, c, and d). The BSE-SEM image (Figure 5b) shows a higher volume fraction of bulk WO_3 crystals in this catalyst sample as compared with 5.2−WZrOH (18.5, 973) catalyst. The average size of the WO_3 particles also increased as the nominal tungsten surface density increased from 5.2 to 8.5 W·nm^{-2}. The significant intensity increase of the m-WO_3 XRD peaks indicated an increased amount of WO_3 crystals.

3.2.4. Catalyst Calcined at Lower Temperature with WO_x Loading Close to Monolayer Coverage. One of the WO_x/ZrO_2 catalysts calcined at a lower temperature of 773 K was also characterized for comparative purposes. The major morphology found in the 4.4−WZrOH (21.7, 773) catalyst was aggregates of small (5−15 nm) ZrO_2 particles. However, they differed from the catalysts calcined at 973 K, in that the ZrO_2 was largely amorphous, according to electron diffraction (Figure 7a) and X-ray diffraction (Figure 2). The ZrO_2 support structure is more clearly shown in the HRTEM image in Figure 7b, where only

Table 2. Brønsted and Lewis Acidity of Supported WO_x/ZrO_2 Catalysts Determined by Pyridine FTIR

Catalyst Sample	Brønsted [μmol·g_{cat}^{-1}]	Lewis [μmol·g_{cat}^{-1}]	Brønsted [sites·W^{-1}]	Lewis [sites·W^{-1}]	B:L ratio
ZrOH (0, 973)	–	29.4	–	–	–
2.5−WZrOH (7.0, 973)	10.3	54.7	0.035	0.183	0.19
3.6−WZrOH (13.2, 973)	20.1	68.0	0.035	0.117	0.29
5.2−WZrOH (18.5, 973)	23.7	64.2	0.027	0.080	0.34
6.0−WZrOH (21.7, 973)	23.7	69.5	0.025	0.073	0.34
8.5−WZrOH (30.0, 973)	24.7	72.9	0.019	0.056	0.34
11.0−WZrOH (32.4, 973)	28.8	52.2	0.019	0.033	0.58
Spent 5.2−WZrOH (18.5, 973)[a]	12.3	61.0	0.016	0.080	0.20
4.4−WZrOH (21.7, 773)	29.5	168.3	0.031	0.175	0.18
8.0−WZrOH (30.0, 773)	30.3	147.7	0.023	0.113	0.21

[a] Postreaction sample collected after 10 h. Reaction conditions: 523 K, 1.04 atm, 1% nC_5 in He. Overall nC_5 conversion <3%.

a very small fraction of the ZrO_2 particles are crystalline in nature as revealed by the occasional localized lattice fringes. HAADF-STEM images were taken from both the amorphous (Figure 7c) and crystalline (Figure 7d) regions of the ZrO_2 support, respectively. Although the speckle contrast from the amorphous ZrO_2 made it slightly more difficult to definitively locate the W atom positions, the WO_x species were seen in Figure 7c to be highly dispersed on the amorphous ZrO_2 support surface as isolated WO_x units and probably as some polytungstate species. In contrast, surface polytungstate was the dominant species found on the crystalline portion of ZrO_2 (Figure 7d), with occasional sub-nm Zr-WO_x clusters also found.

As noted previously[19,32] and also in the present study, the W atoms have a tendency to sit directly above Zr sites on the ZrO_2 surface. Thus, the lack of structural order in the amorphous ZrO_2 support reduced the ability of adjacent W atoms to form a polytungstate network or Zr-WO_x clusters. Previous reports[4,19,32] have suggested that Zr-WO_x clusters and polytungstate species are much more catalytically active than monotungstate species. Therefore, the predominance of the highly dispersed monotungstate WO_x species on the amorphous ZrO_2 surface could be the underlying reason for the extremely low catalytic activity exhibited by this sample. A more crystallized sample with a similar W surface density was found to be more active as a result of the formation of Zr-WO_x clusters and/or polytungstates.

3.2.5. Surface Acidity As a Function of Tungsten Oxide Surface Density. Pyridine FTIR experiments were performed under ultrahigh vacuum conditions and the acquired results represented surface acidity, i.e., the acidic state of the catalyst assessed under nonreaction conditions. The total acidity of the WZrOH(773) and WZrOH(973) series are presented in Table 2.

The surface Brønsted acidity of the WZrOH(973) catalysts, on a per-gram-catalyst basis, increased with ρ_{surf}, correlating to the increasing WO_x content. However, on a per-W-atom basis, the number of B sites was constant at ~0.035 sites·W^{-1} below ML coverage ($\rho_{surf} \approx 4.5$ W·nm^{-2})[4,8,18,27] and decreased gradually above ML coverage; this apparent decrease in acidity resulted from the presence of WO_3 crystals above ML coverage. The B sites to which the pyridine molecule chemisorbed were likely hydroxyl groups (W−O−W−OH or Zr−O−W−OH) associated with W^{6+} and W^{5+} atoms[33,34] depending on the

(32) Zhou, W.; Ross-Medgaarden, E.; Wachs, I. E.; Kiely, C. J. *Microscopy and Microanalysis* **2008**, *14*, 1350–1351.
(33) Di Gregorio, F.; Keller, V. *J. Catal.* **2004**, *225*, 45–55.
(34) Kuba, S.; Heydorn, P. C.; Grasselli, R. K.; Gates, B. C.; Che, M.; Knözinger, H. *Phys. Chem. Chem. Phys.* **2001**, *3*, 146.

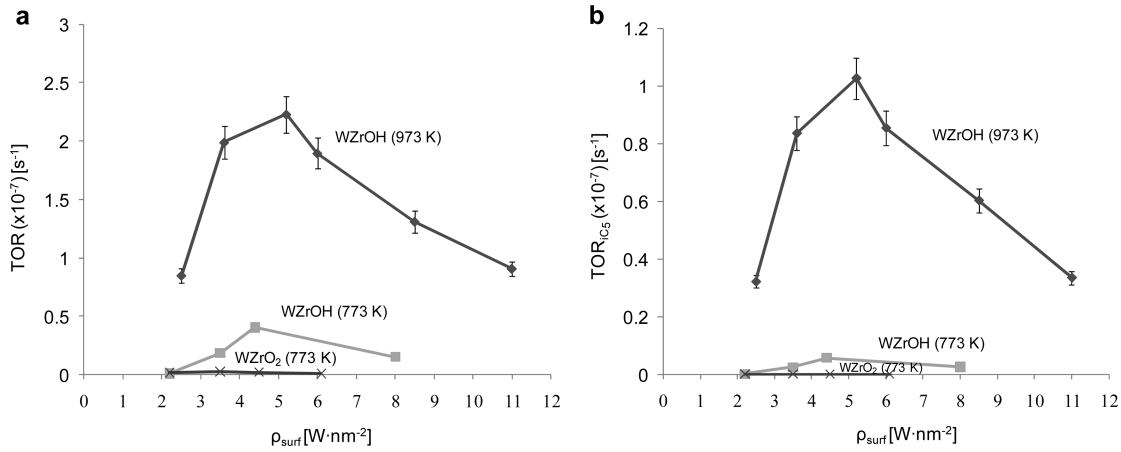

Figure 8. (a) Steady-state nC_5 consumption turnover rates (TOR) and (b) steady-state nC_5 isomerization turnover rates as a function of tungsten surface density. Sample series include (◆) WZrOH(973), (■) WZrOH(773), and (×) $WZrO_2$(773). Reaction conditions: 523 K, 1.04 atm, 1% nC_5 in He. Overall nC_5 conversion <3%.

individual cluster size.[35] In fact, the formation of B sites has been directly correlated to the existence of surface polytungstate species.[5,8,12−18] Calcination at a lower temperature (773 K) slightly increased the number of B acid sites for comparable surface densities in the WZrOH catalysts.

Our observations of B site density compared favorably with results reported by others. Scheithauer et al.[12,13] studied the B acid site amount and strength using low-temperature CO-IR spectroscopy. Based on the carbonyl stretching frequency, B site density reached a maximum above ∼6.0 W·nm^{-2} (which we calculated using the SSA and the WO_3 loading values reported for each sample) and remained unchanged by further increasing ρ_{surf}. Baertsch et al.[16] studied the acidity of WO_x/ZrO_2 catalysts using NH_3−IR spectroscopy combined with temperature-programmed desorption TPD measurements and concluded that the maximum B site density per W atom was found at an intermediate ρ_{surf} of ∼5.5 W·nm^{-2}, which differs from the maximum *o*-xylene isomerization activity observed at $\rho_{surf} \approx 10.0$ W·nm^{-2}. The same group[15] also investigated the *in situ* acidity of WO_x/ZrO_2 by studying its kinetics during 2-butanol dehydration at reaction temperature of 373 K in the presence of pyridine (Py) or 2,6-di-*tert*-butyl-Py. The maximum site density was estimated to be ∼0.04 B sites·W^{-1} and ∼0.04 L sites·W^{-1} at $\rho_{surf} \approx 6.0$ W·nm^{-2}. These results agreed well with the *in situ* B site density (∼0.033 sites·W^{-1}) measured by Santiesteban et al. during nC_5 isomerization in the presence of Py or 2,6-di-*tert*-butyl-Py[8] but were much lower than those reported by Baertsch et al. using NH_3−IR, i.e., 0.2 B sites·W^{-1} and ∼0.08 L sites·W^{-1} at 5.5 W·nm^{-2}.[16] The maximum 2-butanol dehydration rate was similarly observed at $\rho_{surf} \approx 9.0$ W·nm^{-2}, which again did not correspond to the maximum B site density.

The Lewis acidity of WZrOH(973), normalized per gram catalyst, increased significantly with ρ_{surf} up to 8.5 W·nm^{-2} and dropped by 37% at 11.0 W·nm^{-2}. This follows a pattern similar to that for the specific surface area of the catalysts (Table 1). This can be well explained by the fact that the sintering of the parent $ZrO_x(OH)_{4-2x}$ support structure was hindered by a high WO_3 content, yielding more coordinatively unsaturated Zr^{4+} cations that are accessible as L acid surface sites. A lower calcination temperature also led to higher L acid content due to reduced sintering of the support.[5,27]

When normalized to the WO_x surface density, L acid content decreased with increasing ρ_{surf}, which is consistent with previous reports.[12,13,15,16] Whereas B site content decreased slowly with increasing W surface density above 3.6 W·nm^{-2}, L site content decreased more rapidly. Considered in a different way, per W atom, the number of acidic hydroxyl groups decreases more than the number of open Zr sites does, as W content increases.

The B:L ratios were measured to be less than 1 for all samples with the ratio remaining identical between 5.2 and 8.5 W·nm^{-2}. For comparison, Santiesteban et al.[8] reported a "strong" B:L ratio of 1:1 for coprecipitated WO_x/ZrO_2 catalysts and Baertsch et al.[15] reported an *in situ* B:L ratio of 1.75:1 for impregnated WO_x/ZrO_2 materials. The difference in B:L ratio could be due (1) to the difference in catalyst surface environments under reaction or nonreaction conditions; (2) to the difference in material preparation, in which coprecipitated samples have a higher B site density than impregnated ones;[8] (3) to the stronger basicity of 2,6-di-*tert*-butyl-Py compared to Py in the gas phase;[36,37] and (4) to the *in situ* transformation of L to B sites as shown by Baertsch et al. for WO_x/ZrO_2.[16] In addition, during *in situ* characterization the reactant molecule is cofed with the probe molecule, which leads to a competitive chemisorption mechanism that may underestimate the exact number of B and/or L sites.

3.2.6. *n*-Pentane Isomerization Catalytic Activity. 3.2.6.1. Dependence on Surface Density. Steady-state turnover rates (TOR) for all materials are presented in Figure 8. All the WZrOH catalysts demonstrated cracking, isomerization, and oligomerization activity with a TOR maxima at $\rho_{surf} \approx 5.2$ W·nm^{-2}. In contrast, even though the $WZrO_2$ samples calcined at 773 K were reported to possess mild activity for methanol dehydration,[4] they were found to be almost inactive for nC_5 isomerization due to the more demanding acid nature of the nC_5 isomerization reaction. Similarly, bulk WO_3 crystals that are active for methanol dehydration[4] were also found to be inactive for nC_5 isomerization.

For the WZrOH(973) series, both the overall activity (Figure 8a) and isomerization activity (Figure 8b) reached a maximum at 5.2 W·nm^{-2}, correlating well to the large population of Zr-WO_x clusters in this sample as discussed in previous sections. The stronger dependence of isomerization rates on surface

(35) Cortés-Jácome, M. A.; Angeles-Chavez, C.; López-Salinas, E.; Navarrete, J.; Toribio, P.; Toledo, J. A. *Appl. Catal. A: General* **2007**, *318*, 178–189.
(36) Hosmane, R.; Liebman, J. *Struct. Chem.* **2009**, *20*, 693–697.
(37) Hunter, E. P. L.; Lias, S. G. *J. Phys. Chem. Ref. Data* **1998**, *27*, 413–656.

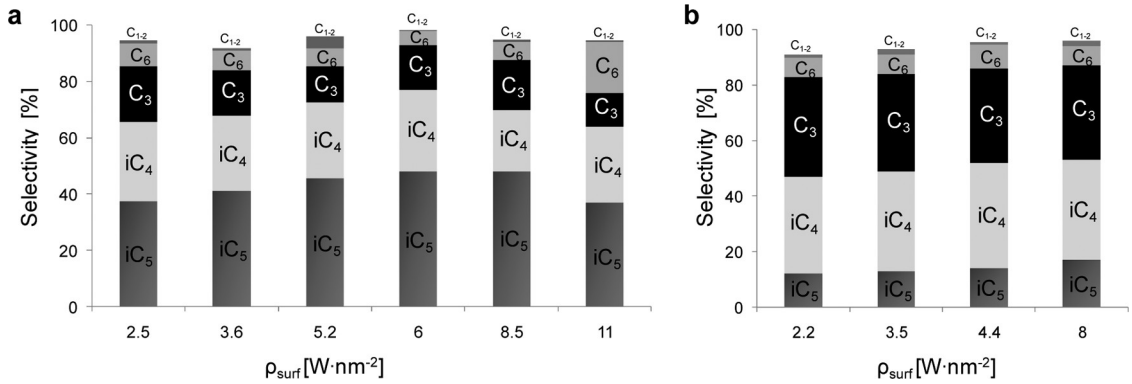

Figure 9. Steady-state product distribution of (a) WZrOH(973) and (b) WZrOH(773). Reaction conditions: 523 K, 1.04 atm, 1% nC_5 in He. Overall nC_5 conversion <3%.

density suggested that these clusters favored the isomerization of *n*-pentane over other acid-catalyzed pathways.

The WZrOH catalysts calcined at 773 K were found to be less active (Figure 8a) and less selective for isopentane (iC_5) formation (Figure 8b). While calcination temperature was not found to impact the activity of WO_x/ZrO_2 for methanol dehydration,[4] 2-butanol dehydration,[15] and *o*-xylene isomerization,[5] it affected WO_x/ZrO_2 catalytic activity for other reactions. For example, Scheithauer et al. reported that WO_x/ZrO_2 calcined at 923 K was ~5 times more active for nC_5 isomerization than those calcined at 1098 K.[12] López et al. reported up to ~5 times higher acetic acid esterification activity for samples calcined at 1073 K in the range 673−1173 K.[38] With our results, such observations show a clear calcination temperature effect, for which the optimum temperature promotes the formation of highly active Zr-WO_x clusters.[4,19]

The selectivity profiles at different surface densities indicate cracking (C_1−C_4), isomerization (iC_5), and oligomerization (>C_6) hydrocarbon products (Figure 9). Carbon mass balances closed at 95−98%, with the remaining carbon mass in the forms of coke precursor (which are more volatile and therefore more easily removable) and hard coke (which are harder to remove, after being formed from further dehydrogenation of the coke precursors).[39] No H_2 was detected, indicating that any H_2 released from cracking reactions was consumed *in situ*.

A monomolecular mechanism was previously proposed for nC_5 isomerization over WO_x/ZrO_2 catalysts under similar reaction conditions.[11] The reaction is initiated via the formation of a carbenium (C_5^+) cation[40] followed by its skeletal isomerization or β-scission[41] to produce iC_5 or C_1−C_4 respectively, similar to what has been reported for zeolite catalysts. The detection of ethane and ethylene (C_2) and traces of methane (C_1) in this study was evidence for a monomolecular cracking mechanism.[42]

Hexane and hexenes (C_6) and traces of higher molecular-weight hydrocarbons were detected in this study also, in accordance with similar studies performed on paraffin cracking over zeolites,[41−45] WO_x/ZrO_2,[9] and sulfated zirconia (SO_4/ZrO_2).[46,47] The detection of species larger than pentane indicates intermolecular transformations were occurring, suggesting that nC_5 isomerization could also occur through a bimolecular reaction pathway. C_6 can be produced from the combination of methyl cation (CH_3^+, generated from D3 β-scission of nC_5[41]) with nC_5. It can also come from a C_{10} surface intermediate formed from the coupling of pentane and pentene molecules, which then cracks into C_6's and C_4's, similar to what has been proposed for SO_4/ZrO_2.[46−49] The same C_{10} intermediate could undergo skeletal isomerization and cracking to generate iC_5. nC_5 isomerization is likely to occur via a bimolecular reaction mechanism for WO_x/ZrO_2, but this point has not been established in literature yet. We are currently studying this in more detail by analyzing the effect of adding alkenes as cofeed.

Selectivity to iC_5 increased from 38% for $\rho_{surf} = 2.5$ W·nm^{-2} to a maximum of 46−48% for ρ_{surf} between 5.2 and 8.5 W·nm^{-2} for the WZrOH catalysts calcined at 973 K (Figure 9a), where the number density of Zr-WO_x clusters also reached a maximum. The isobutane (iC_4) percentage remained constant (~27%) at the surface densities studied. Propane/propylene (C_3) percentages were relatively low at all surface densities except at 2.5 and 3.6 W·nm^{-2}, where their relative concentration increased to 14−20%. C_6 was detected in low amounts at all surface densities except at 11.0 W·nm^{-2}, where its percentage increased to 14%. Small amounts of C_1 and C_2 were detected, with *n*-butane (nC_4) detected in trace amounts (not shown).

The WZrOH samples calcined at 773 K were found to greatly favor cracking over isomerization of nC_5, with iC_5 selectivities remaining below 20% between 2.2 and 8.0 W·nm^{-2} (Figure 9b). iC_4 and C_3 were the main cracking byproducts with their relative concentrations remaining unchanged (~30% and ~25% respectively) at all surface densities. C_6 products were also detected at all surface densities.

WZrOH samples calcined at 973 K were at least twice as good as samples calcined at 773 K as nC_5 isomerization catalysts. We suggest that the surface monotungstate species—found in large amounts in the 773-K-calcined WZrOH samples (Figure 7) but only in small amounts in the 973-K-calcined samples near or above WO_x monolayer coverage promotes

(38) López, D. E.; Suwannakarn, K.; Bruce, D. A.; Goodwin, J. G., Jr. *J. Catal.* **2007**, *247*, 43–50.
(39) Wang, B.; Manos, G. *J. Catal.* **2007**, *250*, 121–127.
(40) Boronat, M.; Viruela, P.; Corma, A. *J. Phys. Chem.* **1996**, *100*, 16514–16521.
(41) Buchanan, J. S.; Santiesteban, J. G.; Haag, W. O. *J. Catal.* **1996**, *158*, 279–287.
(42) Jentoft, F. C.; Gates, B. C. *Top. Catal.* **1997**, *4*, 1–13.
(43) Jolly, S.; Saussey, J.; Bettahar, M. M.; Lavalley, J. C.; Benazzi, E. *Appl. Catal. A: General* **1997**, *156*, 71–96.
(44) Chu, H. Y.; Rosynek, M. P.; Lunsford, J. H. *J. Catal.* **1998**, *178*, 352–362.
(45) Corma, A.; Miguel, P. J.; Orchilles, A. V. *J. Catal.* **1994**, *145*, 58–64.
(46) Lohitharn, N.; Lotero, E.; Goodwin, J. G., Jr. *J. Catal.* **2006**, *241*, 328–341.
(47) Tabora, J. E.; Davis, R. J. *J. Am. Chem. Soc.* **1996**, *118*, 12240–12241.
(48) Kuba, S.; Heydorn, P. C.; Grasselli, R. K.; Gates, B. C.; Che, M.; Knözinger, H. *Phys. Chem. Chem. Phys.* **2001**, 146–154.
(49) Kuba, S.; Lukinskas, P.; Grasselli, R. K.; Gates, B. C.; Knözinger, H. *J. Catal.* **2003**, *216*, 353–361.

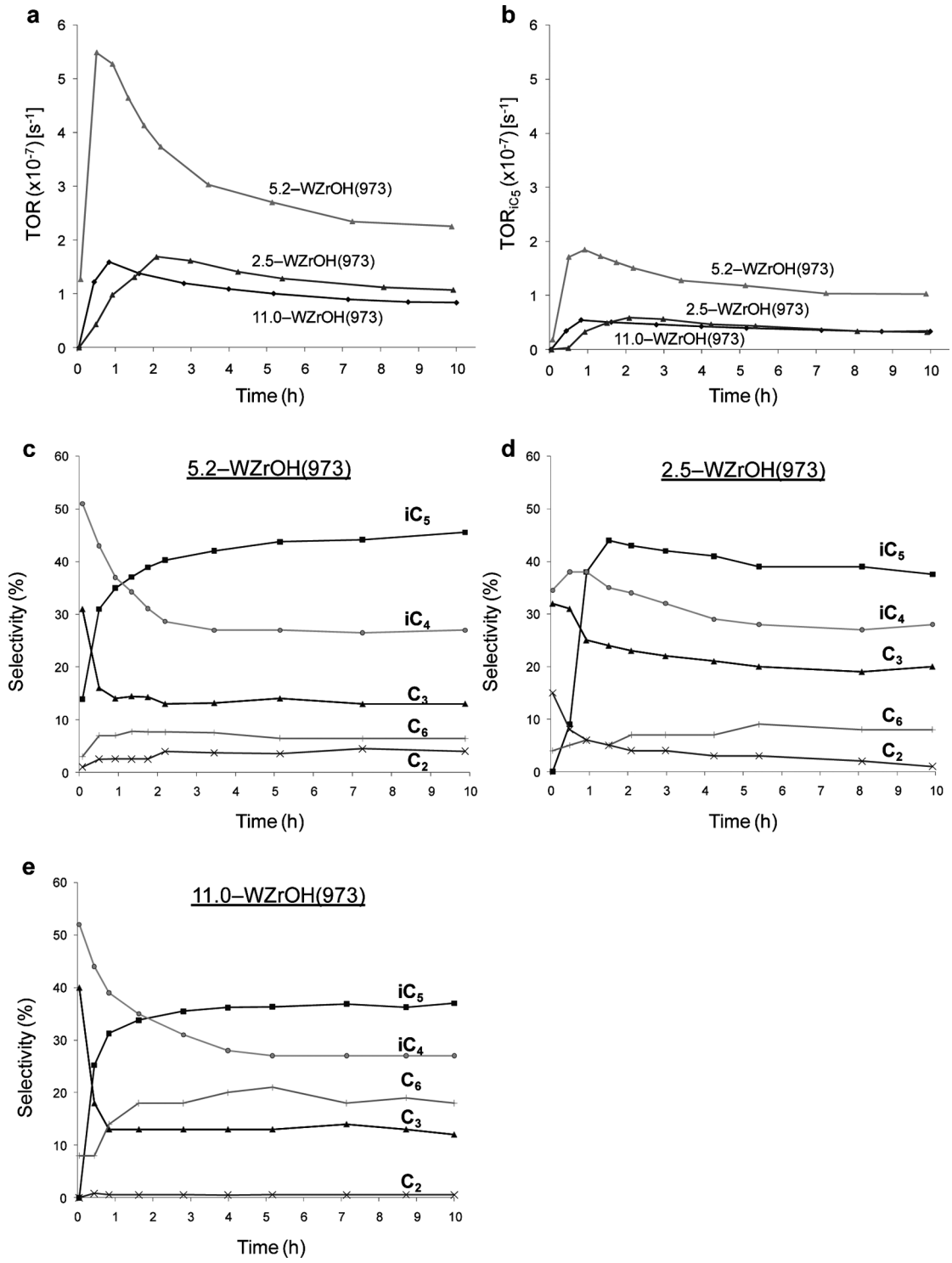

Figure 10. (a) nC_5 transient turnover rates (TOR), (b) transient isomerization turnover rates (TOR_{iC_5}) and product distributions for (c) 5.2−WZrOH (18.5, 973), (d) 2.5−WZrOH (7.0, 973), and (e) 11.0−WZrOH (32.4, 973). Reaction conditions: 523 K, 1.04 atm, 1% nC_5 in He. Overall nC_5 conversion <3%.

monomolecular cracking reaction (Figures 4 and 6). We further suggest that the 0.8−1 nm Zr-WO_x clusters found in the 973-K-calcined samples, with the highest presence near W monolayer coverage, are responsible for bimolecular isomerization activity.

3.2.6.2. Correlation to Surface Acidity. The concentrations of weak, moderate, and strong B sites were comparable for the WZrOH(973) series up to 5.2 $W \cdot nm^{-2}$ (Figure S1a in the Supporting Information). A minor increase in weak B acidity and a small decrease in strong B acidity were noticed in this range, with moderate sites remaining unchanged. High ρ_{surf} decreased moderate and strong B acidity, which corresponded to higher molecular-weight reaction products (Figure 9a). The total B site content of WZrOH(773) material was in line with that of WZrOH(973), on a W surface density basis. No pattern could be discerned from the different B acid strength concentrations (Figure S1a,b) to explain how WZrOH(773) were at least two times less active. As noted earlier, the 773-K-calcined

samples contained more L sites per W than 973 K samples (Table 2, cf. 3.6 and 4.0 $W \cdot nm^{-2}$, and 8.5 and 8.0 $W \cdot nm^{-2}$). No pattern could be discerned from the different L acid strength concentrations either (Figure S1c,d), to explain the differences in catalytic activity.

Recognizing that coke deposition occurred during the reaction that could impact the acid site amount and strengths, we assessed the surface acidity of 5.2−WZrOH (18.5, 973) after 10 h under reaction conditions. Pyridine adsorption FTIR results indicated that the total B acidity decreased from 0.028 to 0.016 sites$\cdot W^{-1}$; the amounts of strong, medium, and weak acid sites proportionally decreased; and the total L acidity remained the same at 0.08 sites$\cdot W^{-1}$ (Figure S2). These observations pointed to the direct participation of B sites during nC_5 isomerization reaction, in agreement with previous reports,[8,15] and suggested that L sites did not participate as active sites.

That the measured B and L site concentrations did not correlate with the observed catalytic activity trends suggested that the catalytically active sites are most likely to form in situ and that the surface tungstate species sites likely generate these active sites during the reaction. This latter point has been considered by several research groups in the context of an observed induction period during flow reactor studies. For WO_x/ZrO_2, the induction period was proposed to result from the *in situ* generation of B sites from L sites.[5,14−16] For the related material SO_4/ZrO_2, the induction period found in *n*-butane skeletal isomerization was attributed to the formation of an oligomeric intermediate via a bimolecular reaction pathway.[46−49]

3.2.6.3. Time-Dependent Catalytic Behavior. Reaction rates and product concentrations were quantified and monitored over 10 h for WO_x/ZrO_2 samples at different surface densities (2.5−WZrOH (7.0, 973), 5.2−WZrOH (18.5, 973), and 11.0−WZrOH (32.4, 973)). In agreement with other reports,[12,49−51] an induction period was observed in all cases, during which the TOR reached a maximum (Figure 10a,b). 5.2−WZrOH (18.5, 973) showed the highest TOR at $\sim 5.5 \times 10^{-7}$ s^{-1} at 1 h, which decreased to a stable value of $\sim 2.0 \times 10^{-7}$ s^{-1} after 7 h. The rapid drop in TOR corresponded with the rapid decrease in iC_4 and C_3 formation (Figure 10c), presumably due to the deactivation of the most active acid sites which favored cracking.[51] C_3 is exclusively produced via a monomolecular mechanism as indicated by the absence of C_7 in the product stream. On the other hand iC_4 can be formed via both a monomolecular and a bimolecular mechanism. The initially high concentration of iC_4 that declines similarly to that of C_3 suggests they share a common monomolecular cracking pathway. The fact that the C_3 concentration drops to the minimum faster (within ~1 h) in contrast to iC_4 that gradually decreases within ~5 h implies a secondary reaction pathway contributing to the formation of iC_4. This bimolecular mechanism generates other iC_4, reaching a steady state concentration within the same time the concentration of C_6 maximizes.

During the 10-h period, TOR_{iC_5} dropped to $\sim 1.0 \times 10^{-7}$ s^{-1} (Figure 10b) but the iC_5 selectivity increased from 14% to 46% for the most active 5.2−WZrOH(18.5, 973) catalyst (Figure 10c), indicating that the acid sites responsible for isomerization were deactivated to a lesser extent. C_6 followed the same trend as iC_5 (Figure 10c), supporting the idea of a common reaction pathway (via a C_{10} intermediate) for these two products and, more specifically, the bimolecular mechanism model for C_5 isomerization.

We speculate that the 5.2−WZrOH(18.5, 973) catalyst, which contains comparable amounts of polytungstate and Zr-WO_x clusters, catalyzes the cracking and isomerization of nC_5. Whereas the polytungstates deactivate immediately with time on stream, the Zr-WO_x clusters undergo an activation process (through partial reduction[48,52]) to form the iC_5-forming B sites. These sites catalyze the bimolecular pathway, leading to the coformation of the observed C_6's, and deactivate with time as the result of C_{10} deposition or oligomerization.

For 2.5−WZrOH and 11.0−WZrOH, the TOR did not increase to the same extent, almost reaching a maximum of 2.0×10^{-7} s^{-1}. This may be due to the smaller populations of polytungstates and Zr-WO_x clusters compared to that of 5.2−WZrOH; the 2.5−WZrOH sample had relatively more monotungstates, and the 11.0−WZrOH had more WO_3 crystals. Whereas the 11.0−WZrOH reached maximum TOR in the same time as 5.2−WZrOH, the lower surface density sample took twice as long to reach maximum TOR (Figure 10a). This observation suggested that the Zr-WO_x clusters took longer to become activated, perhaps due to their being located at the interstices of adjacent small ZrO_2 particles and defect sites (Figure 3d).

4. Conclusions

The pentane isomerization activity of WO_x/ZrO_2 is strongly affected by the nature of the support, calcination temperature, and tungsten oxide surface density. WZrOH samples demonstrated a volcano-shape dependence on tungsten surface density with maximum activity at 5.2 $W \cdot nm^{-2}$, above ML coverage and at the onset of the WO_3 crystallization, in contrast to model $WZrO_2$ that were inactive. The calcination temperature of 973 K, not 773 K, favored the formation of sub-nm Zr-WO_x clusters and in the overall activity of WZrOH, without promoting their surface acidic properties. The induction period during catalysis is critical for the activation of the clusters, which results in the increased isomerization activity and selectivity seen most pronouncedly at intermediate ρ_{surf}. A bimolecular isomerization mechanism, which plays a significant role and requires further investigation, appears to be promoted by these *in situ* activated Zr-WO_x sites.

Acknowledgment. We acknowledge the National Science Foundation (Nanoscale Interdisciplinary Research Team (NIRT), CBET-0609018), SABIC Americas, and 3M (NTF Award) for funding.

Supporting Information Available: Catalyst particle selection; Catalyst characterization; Catalytic studies; Table S1 (Selection of catalyst particle size); Table S2 (Coke content determined by TGA); Figure S1 (Brønsted and Lewis acid site strength as a function of WO_x surface density expressed as sites per W atom); Figure S2 (Amounts of Brønsted and Lewis acid sites of varying acid strengths for 5.2−WZrOH (18.5, 973) before and after the running nC_5 isomerization. This material is available free of charge via the Internet at http://pubs.acs.org.

JA105519Y

(50) De Rossi, S.; Ferraris, G.; Valigi, M.; Gazzoli, D. *Appl. Catal. A: General* **2002**, *231*, 173–184.
(51) Kuba, S.; Knözinger, H. *J. Raman Spectrosc.* **2002**, *33*, 325–332.
(52) Di Gregorio, F.; Keller, N.; Keller, V. *J. Catal.* **2008**, *256*, 159–171.